DE GRUYTER Nanophotonics 2020; 9(12): 3909–3920

Research article

Hodjat Hajian*, Ivan D. Rukhlenko, George W. Hanson, Tony Low, Bayram Butun and Ekmel Ozbay*

Tunable plasmon-phonon polaritons in anisotropic 2D materials on hexagonal boron nitride

https://doi.org/10.1515/nanoph-2020-0080
Received February 2, 2020; accepted March 31, 2020; published online June 1, 2020

Abstract: Mid-infrared (MIR) plasmon-phonon features of heterostructures composing of a plasmonic anisotropic two-dimensional material (A2DM) on a hexagonal boron nitride (hBN) film are analyzed. We derive the exact dispersion relations of plasmon-phonons supported by the heterostructures and demonstrate the possibility of topological transitions of these modes within the second Reststrahlen band of hBN. The topological transitions lead to enhanced local density of plasmon-phonon states, which intensifies the spontaneous emission rate, if the thickness of the hBN layer is appropriately chosen. We also investigate a lateral junction formed by A2DM/hBN and A2DM, demonstrating that one can realize asymmetric guiding, beaming, and unidirectionality of the hybrid guided modes. Our findings demonstrate potential capabilities of the A2DM/hBN heterostructures for active tunable light–matter interactions and asymmetric in-plane polariton nanophotonics in the MIR range.

Keywords: 2D materials; hexagonal boron nitride; hyperbolic; in-plane anisotropy; polaritons; topology.

***Corresponding authors: Hodjat Hajian**, NANOTAM-Nanotechnology Research Center, Bilkent University, 06800, Ankara, Turkey; and **Ekmel Ozbay**, NANOTAM-Nanotechnology Research Center, Bilkent University, 06800, Ankara, Turkey; Department of Electrical and Electronics Engineering, Bilkent University, 06800, Ankara, Turkey; and Department of Physics and UNAM-Institute of Materials Science and Nanotechnology, Bilkent University, 06800, Ankara, Turkey, E-mail: hodjat.hajian@bilkent.edu.tr (H. Hajian); ozbay@bilkent.edu.tr (E. Ozbay)
Ivan D. Rukhlenko: Institute of Photonics and Optical Science (IPOS), School of Physics, The University of Sydney, Camperdown, 2006, NSW, Australia; Information Optical Technologies Centre, ITMO University, Saint Petersburg, 197101, Russia. https://orcid.org/0000-0001-5585-4220
George W. Hanson: Department of Electrical Engineering, University of Wisconsin, 3200 North Cramer Street, Milwaukee, WI, 53211, USA. https://orcid.org/0000-0001-5792-8836
Tony Low: Department of Electrical and Computer Engineering, University of Minnesota, Minneapolis, MN, 55455, USA. https://orcid.org/0000-0002-5759-5899
Bayram Butun: NANOTAM-Nanotechnology Research Center, Bilkent University, 06800, Ankara, Turkey

1 Introduction

The in-plane hyperbolic and elliptic topologies of polaritons produced by various light–matter interactions have spawned many interesting phenomena. These include directional guiding [1–13], nonreciprocal, unidirectional, and asymmetric guiding [14–17], 2D topological transitions [4], the enhancement of local density of states [5–7], planar hyperlensing [6, 8], beaming [9], hyperbolic beam reflection, refraction, and bending [10, 11], negative refraction [12], and the super-Coulombic atom–atom interaction [13]. The hyperbolic topology of equifrequency contours (EFCs) leads to the formation of narrow beams, because a wide range of wavenumbers propagate co-directionally. This contrasts with the more typical circular EFCs of isotropic media, where different wavenumbers propagate in different directions.

Surface plasmon polaritons (SPPs) with in-plane hyperbolic and elliptic topologies have been realized in plasmonic metasurfaces composed of silver [1–3] or graphene [4–6]. These metasurfaces are uniaxial structures in which the signs of the two effective in-plane permittivities or surface conductivities are either opposite or the same. An alternative approach to the realization of the in-plane hyperbolic or elliptic topology is to employ an emerging class of 2D materials with uniaxially anisotropic electronic and optical properties [18]. Such anisotropic 2D materials (A2DMs) includes the group V mono- and multilayers, most notably black phosphorus (BP) [19, 20]. BP is a multilayer plasmonic A2DM with actively tunable electronic and optical properties [21], and thus has found numerous applications in optoelectronics and plasmonics [6, 7, 9–11, 22–30]. SPPs confined to plasmonic metasurfaces or A2DMs exhibit a hyperbolic or figure-eight-like dispersion. This means that their EFCs in the 2D wave vector space are open hyperboloids or closed figure-eight-like contours [1–13, 14–17].

The flat-land optics of in-plane anisotropic polaritons can also be realized with phononic metasurfaces, where photons and optical phonons of polar dielectrics (such as SiC and hexagonal boron nitride, hBN [31, 32]) are coupled into phonon polaritons. hBN is a uniaxially anisotropic $[\underline{\varepsilon_{hBN}} = diag(\varepsilon_t, \varepsilon_t, \varepsilon_z)]$ polar Van der Waals (VdW) material that shows hyperbolic characteristics inside its Reststrahlen (RS) bands in the mid-infrared (MIR) region while acting as a typical anisotropic medium outside of these bands [33, 34]. As a natural hyperbolic material in the RS bands, hBN has dielectric constants that are alike in the basal plane ($\varepsilon_t \equiv \varepsilon_x = \varepsilon_y$) but have opposite signs ($\varepsilon_x\varepsilon_z < 0$) in the normal direction (ε_z). The RS bands of hBN are classified according to their hyperbolic regime as the type-I ($\varepsilon_z < 0$ and $\varepsilon_t > 0$ from 780 to 830 cm^{-1}) and type-II ($\varepsilon_z > 0$ and $\varepsilon_t < 0$ from 1370 to 1610 cm^{-1}) bands [33]. This property allows hBN slabs to support subdiffractional volume-confined hyperbolic phonon polaritons with relatively low losses. Hereafter, the hyperbolic phonon polaritons of bare hBN and guided plasmon-phonon modes of graphene-hBN heterostructures inside (outside) of the RS band of hBN are denoted as HP^2s and HP^3s (SP^3s), respectively [35–38]. As a result, the phonon polaritons in natural hBN exhibit an out-of-plane hyperbolic dispersion while their in-plane dispersion is isotropic. An in-plane anisotropic phononic response can be achieved in metasurfaces that are created by lateral structuring of thin layers of isotropic or anisotropic dielectrics with a high degree of ionicity such as SiC or hBN [39]. This response is also exhibited by 2D phononic materials with a natural in-plane anisotropy such as α-MoO_3 [40, 41].

HBN ideally complements A2DM in hybrid structures, due to its large bandgap (6 eV), high mechanical strength, high thermal stability, and chemical inertness [42, 43]. Recently, in-plane anisotropic phonon polaritons have been directly observed in a VdW hBN/BP heterostructure with an undoped BP film as a buffer layer [44]. It was shown that the highly confined phonon polaritons of hBN allow one to significantly enhance the in-plane optical anisotropy along the armchair and zigzag crystal axes. Indeed, the interplay between the hyperbolic phonon-polaritons in hBN and that of anisotropic plasmon-polaritons would strongly influence the character of the hybrid polaritons. However, the exact dispersion relation of these hybrid guided modes have not been investigated to-date.

This paper presents the exact dispersion relations for the guided SP^3s and HP^3s modes supported by an A2DM/hBN/sub heterostructure, where "sub" denotes substrate. These relations are then simplified to the case of an A2DM/sub structure to investigate the effect of substrate on the modal properties of SPPs supported by the plasmonic A2DM, which are denoted here as SP^2s [35, 37, 38]. We calculate the EFCs, density plots, and electric field distributions of the guided modes supported by a suspended A2DM, A2DM/sub, and A2DM/hBN/sub heterostructures to analyze how the presence of hBN can lead to the topological transition of the guided modes. This analysis is followed by the calculation of the spontaneous emission rates (SERs) of a point source located in the vicinity of the A2DM/sub and A2DM/hBN/sub systems for different thicknesses of hBN layer. Finally, we discuss the observation of the induced asymmetry effects of the guided modes supported by a uniform A2DM sheet when the A2DM/sub and A2DM/hBN/sub systems are laterally combined in a double heterostructure. It is shown that the induced asymmetry leads to asymmetric guiding, beaming, and unidirectionality of the guided modes supported by the heterostructure.

2 Physical model

The analysis of exact dispersion relations is a powerful tool for the investigation of the modal properties of guided modes supported by photonic waveguides [45–47]. The dispersion relation of a free-standing A2DM sheet [Figure 1(a)] is thoroughly analyzed while the effect of the substrate, most notably on hBN due to their widespread use in 2D materials, has received little attention. We therefore begin our study by deriving an exact dispersion relation of hybrid modes supported by an A2DM/hBN/sub structure [Figure 1(c)]. A simpler A2DM/sub structure [Figure 1(b)] is also considered as a special case. It should be noted that, for illustrative purposes, a BP sheet with puckered structure represents the A2DM sheet in the schematics shown in Figure 1.

As schematically shown in Figure 1(c), an hBN film of thickness l rests on a substrate with refractive index $n_s = 1.5$ and covered by an A2DM sheet with optical conductivity $\underline{\boldsymbol{\sigma}} = \text{diag}(\sigma_{xx}, \sigma_{yy})$. Here [10]

$$\sigma_{jj} = \frac{ie^2}{\omega + i\eta}\frac{n}{m_j} + s_j\left(\Theta(\omega - \omega_j) + \frac{i}{\pi}\ln\left|\frac{\omega - \omega_j}{\omega + \omega_j}\right|\right), \qquad (1)$$

n is the concentration of electrons, m_j is the effective mass of electrons along the jth direction, and η is the relaxation time. This minimal model for a 2D anisotropic semiconducting medium accounts for both the intraband

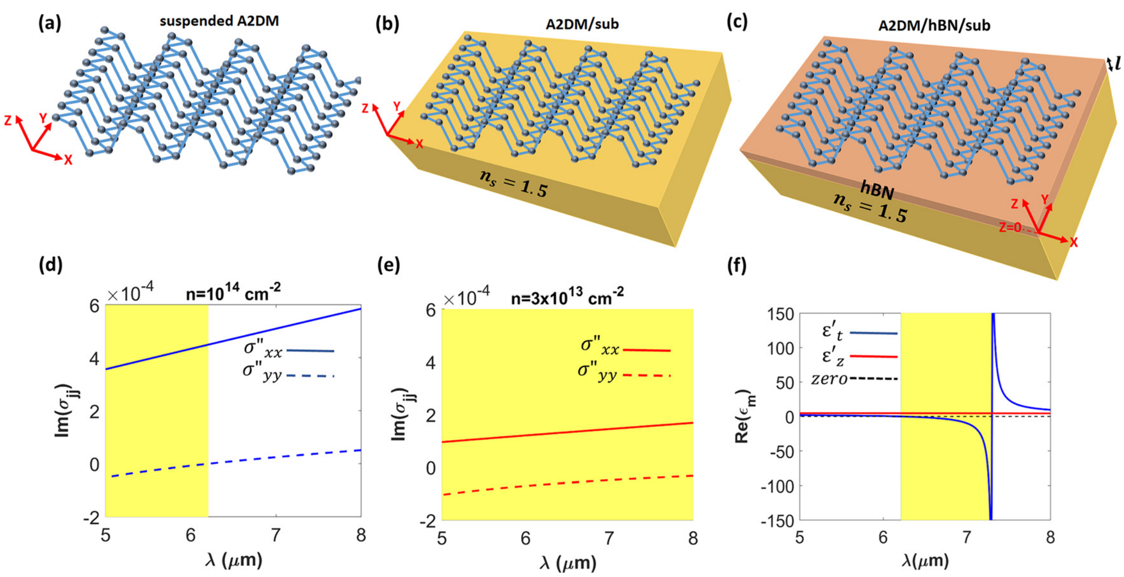

Figure 1: [(a)–(c)] Suspended A2DM sheet, A2DM/sub structure, and A2DM/hBN/sub structure; for illustrative purposes, in panels [(a)–(c)] a BP layer with puckered structure represents the A2DM sheet; (d) and (e) imaginary part of the *xx* (solid curves) and *yy* (dashed curves) components of the optical conductivity tensor of the considered A2DM for $n = 10^{14}$ cm^{-2} and $n = 3 \times 10^{13}$ cm^{-2}; (f) real part of the transversal (blue curve) and *z* (red curve) components of hBN permittivity where the extra dotted line indicates zero values of the permittivity; shaded regions in panels (d)–(f) highlight the hyperbolic regions.

electron transitions (through the first term) and the interband electron transitions (phenomenologically described by the step function, Θ); ω_j is the frequency of the onset of interband transitions for the *j*th component of the conductivity tensor and s_j accounts for the transition rate. It should be noted that the case of $m_x \neq m_y$ corresponds to anisotropic response, and the interplay between the intraband and interband processes and their anisotropic response is responsible for the observation of the hyperbolic optical response of A2DM at certain wavelengths. Here, we consider the following material parameters: $m_x = 0.2\, m_0$, $m_y = m_0$ (m_0 is the mass of a free electron), $\eta = 0.01$ eV, $\omega_x = 1$ eV, $\omega_y = 0.35\, eV$, $s_x = 1.7\, s_0$, $s_y = 3.7\, s_0$, and $s_0 = e^2/4\hbar$ [10]. It should be noted that the parameters used in Eq. (1) may be fitted in a way that equation represents experimental results related to BP or other type of anisotropic semiconducting 2D materials.

Figure 1(d) shows the imaginary part of the *xx* and *yy* components of the optical conductivity of the A2DM for $n = 10^{14}$ cm^{-2} (blue curves) and $n = 3 \times 10^{13}$ cm^{-2} (red curves) over the wavelength range from 5 μm (2000 cm^{-1}) to 8 μm (1250 cm^{-1}) covering the type-II RS band of hBN. The tuning of electron concentration is typically achieved experimentally via a back or top gate [21]. According to the figure, the A2DM acts as a natural hyperbolic material with $\sigma''_{xx}\sigma''_{yy} < 0$ for $\lambda < 6.22\,\mu$m when $n = 10^{14}$ cm^{-2} and for all λ from the domain of interest (5 – 8 μm) for $n = 3 \times 10^{13}$ cm^{-2}.

The permittivity tensor of hBN, $\underline{\boldsymbol{\varepsilon}_{hBN}} = \mathrm{diag}(\varepsilon_t, \varepsilon_t, \varepsilon_z)$, is given by

$$\varepsilon_m = \varepsilon_{\infty,m}\left(1 + \frac{\omega_{LO,m}^2 - \omega_{TO,m}^2}{\omega_{TO,m}^2 - \omega^2 - i\omega\Gamma_m}\right), \tag{2}$$

where $m = t$ or z, $\varepsilon_{\infty,t} = 2.95$, $\varepsilon_{\infty,z} = 4.87$, $\omega_{LO,t} = 1610$ cm^{-1} (6.21 μm), $\omega_{TO,t} = 1370$ cm^{-1} (7.3 μm), $\omega_{LO,z} = 830$ cm^{-1}, $\omega_{TO,z} = 780$ cm^{-1}, $\Gamma_t = 4$ cm^{-1}, and $\Gamma_z = 5$ cm^{-1} [33]. Hence, hBN is a natural hyperbolic material within its type-II RS band as shown in Figure 1(e).

In order to derive the dispersion relation of the guided modes supported by the A2DM/hBN/sub structure, we take the electric field to be of the form $\boldsymbol{E}(x, y, z, t) = \boldsymbol{E}(z)e^{i(\beta_x x + \beta_y y - \omega t)}$. Within the hBN layer, $\boldsymbol{E}(z)$ is a linear combination of ordinary (o) and extraordinary (e) waves, and in the entire structure the electric field is given by

$$\boldsymbol{E}(z) = \begin{cases} \boldsymbol{E}_+ e^{-q_a(z-l/2)}\,; z > l/2 \\ \boldsymbol{E}_+^o e^{q_o z} + \boldsymbol{E}_-^o e^{-q_o z} + \boldsymbol{E}_+^e e^{q_e z} + \boldsymbol{E}_-^e e^{-q_e z}\,; |z| < l/2 \\ \boldsymbol{E}_- e^{q_s(z+l/2)}\,; z < -l/2 \end{cases} \tag{3}$$

where

$$\boldsymbol{E}_\pm = \left(E_{\pm x}, E_{\pm y}, \pm\frac{i}{q_{a,s}}\left(\beta_x E_{\pm x} + \beta_y E_{\pm y}\right)\right), \tag{4a}$$

$$\boldsymbol{E}_{\pm}^{o} = E_{\pm}^{o}\left(\beta_y,\ -\beta_x,\ 0\right), \tag{4b}$$

$$\boldsymbol{E}_{\pm}^{e} = E_{\pm}^{e}\left(\mp\frac{i\beta_x q_e}{\varepsilon_t\beta_0},\ \mp\frac{i\beta_y q_e}{\varepsilon_t\beta_0},\ -\beta_0-\frac{q_e^2}{\varepsilon_t\beta_0}\right), \tag{4c}$$

and we have introduced the following parameters: $q_a=\sqrt{\beta^2-\varepsilon_a\beta_0^2}$, $q_s=\sqrt{\beta^2-\varepsilon_s\beta_0^2}$, $q_o=\sqrt{\beta^2-\varepsilon_t\beta_0^2}$, $q_e=\sqrt{(\varepsilon_t/\varepsilon_z)(k^2-\varepsilon_z\beta_0^2)}$, $\beta^2=\beta_x^2+\beta_y^2$, and $\beta_0=\omega/c$.

By applying the boundary conditions [48]

$$\begin{cases}\hat{z}\times(\boldsymbol{H}_1-\boldsymbol{H}_2)=\underline{\boldsymbol{\sigma}}\cdot E\\ \hat{z}\times(\boldsymbol{E}_1-\boldsymbol{E}_2)=0\end{cases}, \tag{5}$$

and after some algebra, we arrive at the dispersion relation of the guided plasmon-phonon modes supported by the A2DM/hBN/sub structure in the form

$$\tan h(q_e l) = -A/B, \tag{6}$$

where coefficients A and B are given in the Supporting Information.

An alternative approach to the analysis of the EFCs of the guided modes supported by the A2DM/hBN/sub structure is to employ the transfer matrix method (TMM) and calculate the transmission of light with different wavenumbers. The density plot of the transmission coefficient shows which wavenumbers in the EFC are primarily responsible for the excitation of the guided modes.

In order to calculate the transmission coefficient, we denote the incident, reflected, and transmitted electric fields as $\boldsymbol{E}_{+,i}$, $\boldsymbol{E}_{+,r}$, and $\boldsymbol{E}_{-,t}$ and re-write Eq. (3) as

$$\boldsymbol{E}(z)=\begin{cases}\boldsymbol{E}_{+,i}e^{q_a((z-l/2)}+\boldsymbol{E}_{+,r}e^{-q_a(z-l/2)};\ z>l/2\\ \boldsymbol{E}_{+}^{o}e^{q_o z}+\boldsymbol{E}_{-}^{o}e^{-q_o z}+\boldsymbol{E}_{+}^{e}e^{q_e z}+\boldsymbol{E}_{-}^{e}e^{-q_e z};\ |z|<l\\ \boldsymbol{E}_{-,t}e^{q_s(z+l/2)};\ z<-l/2\end{cases} \tag{7}$$

where

$$\boldsymbol{E}_{+,i}=\left(E_{+x,i},\ E_{+y,i},\ \frac{-i}{q_a}\left(\beta_x E_{+x,i}+\beta_y E_{+y,i}\right)\right), \tag{8a}$$

$$\boldsymbol{E}_{+,r}=\left(E_{+x,r},\ E_{+y,r},\ \frac{+i}{q_a}\left(\beta_x E_{+x,r}+\beta_y E_{+y,r}\right)\right), \tag{8b}$$

and

$$\boldsymbol{E}_{-,t}=\left(E_{-x,t},\ E_{-y,t},\ \frac{-i}{s}\left(\beta_x E_{-x,t}+\beta_y E_{-y,t}\right)\right) \tag{8c}$$

By applying the boundary conditions, we arrive at the following matrix equation:

$$\begin{pmatrix}E_{+x,i}\\E_{+y,i}\\E_{+x,r}\\E_{+x,r}\end{pmatrix}=M\begin{pmatrix}E_{-x,t}\\E_{-y,t}\end{pmatrix}, \tag{9}$$

in which

$$M=NO^{-1}PQ^{-1}=\begin{pmatrix}M_{11}&M_{12}\\M_{21}&M_{22}\\M_{31}&M_{32}\\M_{41}&M_{42}\end{pmatrix} \tag{10}$$

and N, O, P, and Q are the matrices given in the Supporting Information. From Eqs. (8)–(10) we find

$$E_{-x,t}=\frac{M_{22}E_{+x,i}-M_{12}E_{+y,i}}{M_{11}M_{22}-M_{12}M_{21}}, \tag{11a}$$

$$E_{-y,t}=-\frac{M_{21}E_{+x,i}-M_{11}E_{+y,i}}{M_{11}M_{22}-M_{12}M_{21}}, \tag{11b}$$

and get the transmission coefficient of the A2DM/hBN/sub structure in the form

$$T=\frac{\left|E_{-x,t}\right|^2+\left|E_{-y,t}\right|^2+\left|\beta_x E_{-x,t}+\beta_y E_{-y,t}\right|^2/q_s^2}{\left|E_{+x,i}\right|^2+\left|E_{+y,i}\right|^2+\left|\beta_x E_{+x,i}+\beta_y E_{+y,i}\right|^2/q_a^2}. \tag{12}$$

We are also interested in analyzing the effect of the substrate on the modal characteristics of a single A2DM sheet. By taking the limits $l\to 0$ and $\varepsilon_t,\ \varepsilon_z\to\varepsilon_s$ in Eq. (6), we arrive at the dispersion relation of SPPs supported by the A2DM/sub structure [Figure 1(b)]

$$A_3+B_6-q_o^2\epsilon_0\varepsilon_a\beta_0=-q_a A_5, \tag{13}$$

where A_3, A_5, and B_6 are given in the Supporting Information.

Setting $\varepsilon_s=\varepsilon_a=1$ in the last equation, yields the following well-known dispersion relation of SPPs of a suspended A2DM sheet [5–7, 10, 11, 48]:

$$iq_a\beta_0\left(\sigma_{xx}\sigma_{yy}+\frac{4\epsilon_0}{\mu_0}\right)=2\sqrt{\frac{\epsilon_0}{\mu_0}}\left[\beta_x^2\sigma_{xx}+\beta_y^2\sigma_{yy}-(\sigma_{xx}+\sigma_{yy})\beta_0^2\right]. \tag{14}$$

The transmission-coefficient approach will be used to analyze the EFCs of the A2DM/sub structure and the suspended A2DM sheet.

3 Results and discussion

3.1 Modal characteristics of SPPs supported by a suspended A2DM

We proceed to investigate the impact of substrate on the modal properties of A2DM SPPs. In order to study the properties of surface modes in materials and structures with in-plane anisotropy, we analyze EFCs $\omega(\beta_x, \beta_y) = \text{const}$ rather than plasmon dispersion $\boldsymbol{\beta}(\omega)$. The reason is that the direction of the mode wavefront propagation in anisotropic systems, defined by wavevector $\boldsymbol{\beta}$, does not generally coincide with the direction of energy flow, defined by the group velocity $\nabla_{\boldsymbol{\beta}}\omega(\boldsymbol{\beta})$ [15]. From the property of the gradient operator it follows that the surface mode in anisotropic materials carries energy in the directions orthogonal to the EFCs.

The EFCs, density plots, and electric fields associated with SPPs supported by a suspended A2DM sheet are shown in Figure 2. The subscripts 1, 2, and 3 of the letters marking the panels of the figure distinguish between the results obtained for $\lambda = 5$, 6.5, and 8 μm, respectively (and similar in Figure 3, Figures S2, and S3). In Figures 2, 3 and Figure S2 the concentration of electrons in the A2DM is 10^{14} cm^{-2}. Moreover, for all numerical calculations in this paper, the z-polarized electric dipole is located at x = y = 0, 10 nm away from surface of the structures and the top-view mode profiles are calculated at a plane 5 nm way from the structures surface.

In agreement with Figure 1(d), at 5 μm (2000 cm^{-1}), $\sigma''_{xx} = 3.56 \times 10^{-4}$ S and $\sigma''_{yy} = -5.22 \times 10^{-5}$ S, thus $|\sigma''_{xx}/\sigma''_{yy}| = 6.82$ and $\sigma''_{xx}\sigma''_{yy} < 0$. In this case, only one component of the conductivity tensor is of metallic type and, consequently, A2DM supports SPPs with hyperbolic topology at this wavelength [Figure 2(a$_1$)]. For the suspended A2DM sheet, the hyperbola's asymptotes can be obtained from Eq. (14) by assuming that $\beta_x, \beta_y \gg \beta_0$ and neglecting the losses [10, 11, 15],

$$\frac{q_y}{|q_x|} = \pm\sqrt{\left|\frac{\sigma''_{xx}}{\sigma''_{yy}}\right|}. \tag{15}$$

The density plot of the transmission coefficient of the suspended A2DM sheet for $\lambda = 5$ μm is shown in Figure 2(b$_1$). A good agreement between the EFC and the trend of the density plot can be seen. It is also observed that the wavenumbers that satisfy the

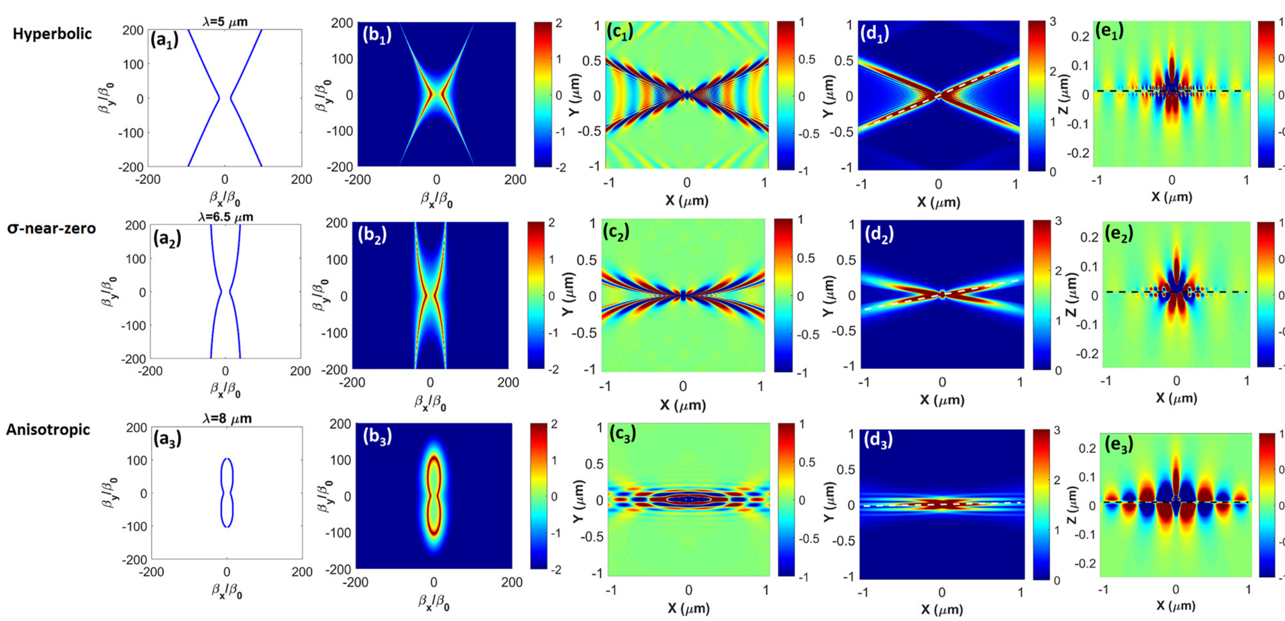

Figure 2: (a$_i$) EFCs, (b$_i$) transmission coefficients, and [(c$_i$)–(e$_i$)] density plots of electric fields associated with SPPs supported by a suspended A2DM sheet [Figure 1(a)] with $n = 10^{14}$ cm^{-2}; (c$_i$) and (d$_i$) are the top-view spatial distributions of Re(E_z) and $|E_z|$, respectively, and (e$_i$) are the side-view of the field. The panels denoted by subscripts 1, 2, and 3 correspond to $\lambda = 5$ μm, 6.5 μm and 8 μm, respectively; dashed horizontal line shows the location of the A2DM sheet.

condition $(|\beta_x|, |\beta_y|) < (65\,\beta_0, 125\,\beta_0)$ are mostly responsible for the strong excitation of the SPPs. The top views of the $\mathrm{Re}(E_z)$ and $|E_z|$ field distributions, shown in Figure 2(c_1) and (d_1), clearly demonstrate the hyperbolic directional guiding of the SPPs. More specifically, the white dashed line in Figure 2(d_1) indicates that the SPP ray travels along the suspended A2DM sheet at an angle of $\varphi = 24.7°$ with respect to the x axis. This value is in good agreement with the one predicted by the asymptotic behavior

$$\frac{y}{|x|} = \pm\sqrt{\left|\frac{\sigma''_{yy}}{\sigma''_{xx}}\right|}, \tag{16}$$

which gives the normals to the asymptotes and thus a good estimation of the group velocity direction of the SPPs supported by a suspended A2DM sheet. The angle that the SPP propagation direction makes with the x axis is seen to increase as the operation wavelength becomes smaller (for example, $\varphi = 36.87°$ for $\lambda = 4$ μm). As explained in Section C of the Supporting Information, this angle can be actively tuned by changing the concentration of electrons in the A2DM.

An even more interesting scenario arises in the purely anisotropic regime (i.e., for $\sigma''_{xx} > 0$ and $\sigma''_{yy} > 0$) when one of the imaginary components of A2DM conductivity tensor dominates over the other (e. g., $\sigma''_{xx} \gg \sigma''_{yy}$). This regime is characterized by the support of SPPs with an anisotropic elliptic or figure-eight-like topology which favors propagation in specific directions. With this topology, A2DM can canalize most of the plasmon energy toward the x axis due to low values of σ''_{yy}. The first example of the considered topology for $\lambda = 6.5$ μm ($\sigma''_{xx} \approx 7.16\,\sigma''_{yy}$) is shown in Figure 2($a_2$)–($e_2$). Due to relatively small σ''_{yy}, this case is also called a σ-near-zero regime [6]. The comparison of Figure 2(a_2) and (a_1) shows that the change of dispersion from hyperbolic to σ-near-zero leads to a noticeable modification of the EFC. According to Figure 2(b_2), all the wavenumbers in the EFC contour with $(|\beta_x|, |\beta_y|) < (67\,\beta_0, 127\,\beta_0)$ correspond to high densities in the transmission plot.

The top-view profiles of $\mathrm{Re}(E_z)$ and $|E_z|$ are shown in Figure 2(c_2) and (d_2). The value of φ corresponding to the dashed white line in the $|E_z|$ profile is 11.86°. In this instance the group velocity points predominantly along the directions that make smaller angles with the horizontal axis as compared to the case of $\lambda = 6.5$ μm. Thus, SPPs carry energy in the form of narrow rays propagating almost parallel to the x axis [15].

Figure 2(a_3)–(e_3) correspond to $\lambda = 8$ μm when $\sigma''_{xx} \gg \sigma''_{yy}$ but σ''_{yy} is less smaller than σ''_{xx} compare to the previous case ($\sigma''_{xx} \approx 3.39\,\sigma''_{yy}$), thus this case is called as anisotropic regime. Now the material is less anisotropic than for $\lambda = 6.5\,\mu m$, and the figure-eight-like shapes appear in the respective EFC [Figure 2(a_3)] and density plot [Figure 2(b_3)]. Notice that since the ratio $\sigma''_{xx}/\sigma''_{yy}$ is now smaller than before, the figure-eight-like EFC correspond to smaller values of β_y/β_0 [10, 15]. Much like for $\lambda = 6.5$ μm, all the wavenumbers in the EFC contour for $\lambda = 8\,\mu m$ take high density values indicating that they all can be involved in the mode excitation. Moreover, the top-view of the $\mathrm{Re}(E_z)$ field [Figure 2(c_3)] suggests that the spatial distribution of the electric field at this wavelength is significantly modified as compared to the previous cases. The latter observation is supported by the $|E_z|$ field distribution in Figure 2(d_3). For the dashed white line, the direction of the group velocity with respect to the x axis is given by the angle $\varphi = 1.43°$. This value indicates that the SPPs carry energy in the form of subdiffractional rays propagating along the x axis, which in the present case is the crystallographic axis of A2DM.

It should be noted that Figures 2(e_j), 3(e_j), and 4(e_j) for $j = 1, 2, 3$ show $\mathrm{Re}(E_z(x, z))$ in the plane $y = 0$. As discussed earlier, SPPs of an A2DM sheet propagate in the x and y directions with hyperbolic, σ-near-zero, and anisotropic dispersions. The side-view mode profiles in panels (e_j) allow one to estimate the strengths of the SPPs localization in the structure in all these cases.

We note that the effect of an underlying trivial substrate is minimal, and we defer their analysis to the Supporting Information. Hereinafter, the SPPs of the suspended A2DM sheet and the A2DM/sub structure are simply denoted as SP^2s.

3.2 Hybrid guided modes supported by an A2DM/hBN/substrate heterostructure

Besides being compatible with an A2DM, hBN has a very useful phononic property in the MIR range — it behaves as a natural hyperbolic material within its RS bands and as a uniaxially anisotropic dielectric with low-losses outside of them [33–39]. In this section we analyze an A2DM/hBN/sub heterostructure [Figure 1(c)] which is more functional than the suspended A2DM sheet and the A2DM/sub structure considered earlier. The comparison of shaded regions in Figure 1(e) and (f) shows that the wavelength domain from 5 to 8 μm contains both hyperbolic regions of the A2DM with $n = 3 \times 10^{13}$ cm^{-2} and the type-II RS band of hBN. Note that these hyperbolic regions of A2DM and hBN do not overlap for $n = 10^{14}$ cm^{-2}, as seen from Figure 1(d) and (f). In the following calculations thickness of the hBN film, l, is taken as it is assumed that 20 nm unless stated otherwise.

It is well-known that once hBN is combined with a 2D plasmonic material such as graphene that supports SPPs or SP²s, the resulting structure supports hybrid plasmon-phonon modes which are combinations of SP²s and HP²s and may be referred to as SP³s and HP³s outside of the RS band and inside this band, respectively [35, 37, 38]. Here we use the same notations for the modes supported by our structure. The EFC diagram and the transmission coefficient associated with the A2DM/hBN/sub heterostructure at $\lambda = 5$ μm are shown in Figure 3(a$_1$) and (b$_1$). The dispersion of SP²s supported by the suspended A2DM sheet (solid blue curve) and the A2DM/sub structure (solid red curve) are also shown for reference. One can see that when hBN acts as a uniaxially anisotropic dielectric, the SP³s dispersion is almost the same as the dispersion of SP²s in the A2DM/sub heterostructure. Similarly, the wavenumbers that are mostly involved in the excitation of the mode satisfy the condition $(|\beta_x|, |\beta_y|) < (80\,\beta_0, 120\,\beta_0)$.

The analysis of EFCs at other wavelengths shows that when hBN is used as a buffer layer, the guided plasmon-phonons possess modal features that are typical for the modes supported by the A2DM/sub structure at wavelengths below the edge wavelength of the type-II RS band of hBN, $\lambda \leq 6.2$ μm (as explained below, topological transitions occur for the guided modes within the type-II RS band of hBN). This claim is supported by the observation from the Re(E_z) field distribution [Figure 3(c$_1$)] that the SP³ mode travels in the plane of the A2DM sheet with a profile similar to the one shown in Figure S2(c$_1$). In particular, in agreement with Figure S2(a$_1$), the angle of ray propagation with respect to the x axis, $\varphi = 25.64°$, calculated from the dashed white line in Figure 3(d$_1$), is exactly the same as that for the A2DM/sub structure. The comparison of $|E_z|$ in Figure 3(d$_1$) and Figure S2(d$_1$) also shows that for $\lambda = 5$ μm the SP³ mode propagates along the A2DM/hBN/sub heterostructure as far as the SP² mode along the A2DM/sub structure, which means that the decay lengths in both cases are almost the same.

The topological features of HP³s within the type-II RS band of hBN at $\lambda = 6.5$ μm differ significantly from the features of SP²s in the suspended A2DM sheet and the A2DM/sub structure. The EFC of the guided mode at this wavelength [Figure 3(a$_2$)] is a mixture of the figure-eight-like dispersion of the A2DM SP²s and elliptic/circular dispersion of the hBN HP²s; therefore, we label it as HP³. The density plot in Figure 3(b$_2$) shows that all the wavenumbers in the EFC diagram are responsible for the excitation of the guided mode. This point was observed in the density plots of SP²s of the suspended A2DM sheet

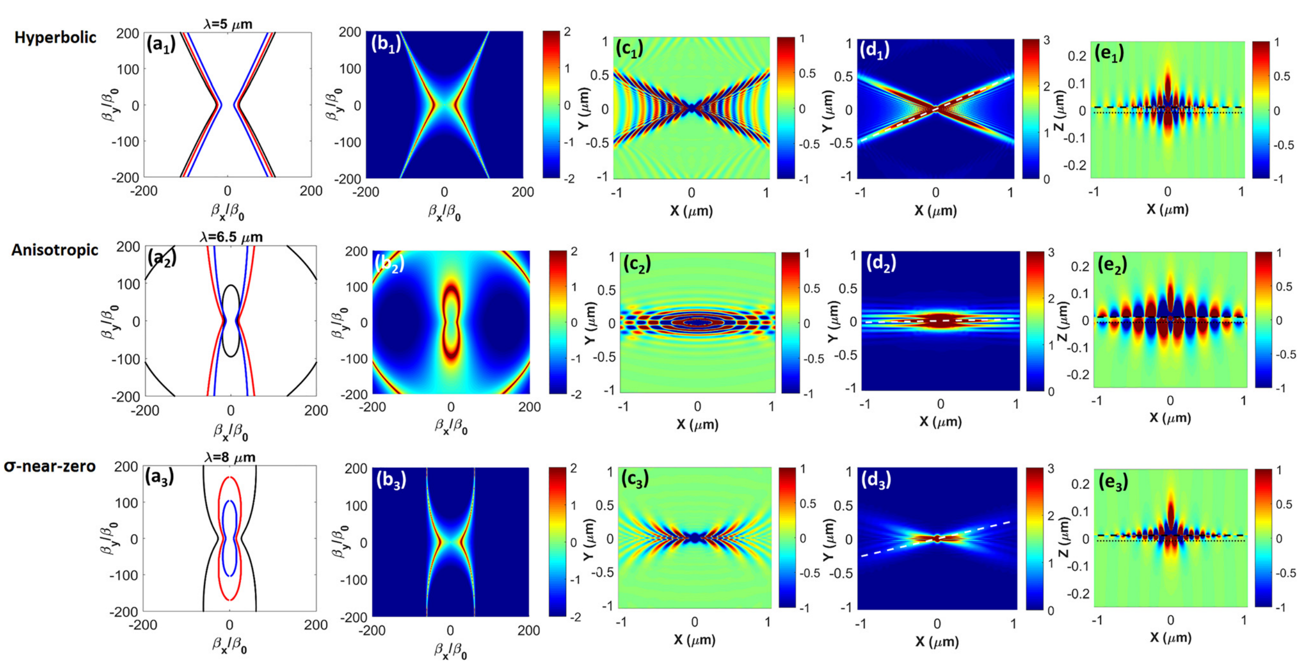

Figure 3: (a$_i$) EFCs, (b$_i$) transmission coefficients, and [(c$_i$)–(e$_i$)] density plots of electric field associated with the guided modes supported by the A2DM/hBN/sub structure [Figure 1(c)] with $n = 10^{14}$ cm^{-2}. The meaning of panels (c$_i$)–(e$_i$) is the same as in Figure 2. Black curves in (a$_i$) are the guided modes of the A2DM/hBN/sub structure whereas blue and red curves correspond to the SP²s of the suspended A2DM sheet and the A2DM/sub structure, respectively. Dotted horizontal line in (e$_i$) shows the interface between the hBN layer and the substrate.

[Figure 2(b_3)] at $\lambda = 8$ μm, confirming the change in the topology of the HP3 mode in the type-II RS band due to the presence of hBN. In fact, the topology of HP^3 is anisotropic (not σ-near-zero) at this wavelength. This is further evidenced by the fact that $\mathrm{Re}(E_z)$ and $|E_z|$ of the HP^3 mode at $\lambda = 6.5$ μm [Figure 3(c_2) and (d_2)] resemble similar field distributions of the suspended A2DM sheet SP^2s at $\lambda = 8$ μm. Besides, the angle of ray propagation with respect to the x axis calculated from Figure 3(d_2), $\varphi = 1.38°$, is very close to the value 1.43° found from Figure 2(d_3).

More investigations reveal that at the lower boundary of the type-II RS band, $\lambda = 6.2$ μm, the dispersion topology of the guided mode supported by the A2DM/hBN/sub structure is σ-near-zero, similar to the one of the A2DM SP^2 at 6.5 μm [Figure 2(a_2)–(e_2)]. At the boundary frequency, the SP^3s of the A2DM/hBN/sub structure are characterized by $\varphi = 11.86°$, which is the same as for the suspended A2DM sheet SP^2s at $\lambda = 6.5$ μm.

Similarly, at other wavelengths outside of the type-II RS band of hBN, e. g., $\lambda = 8$ μm, the topology of the SP^3 mode of the A2DM/hBN/sub structure differs from the topologies of the SP^2 modes of the suspended A2DM sheet and the A2DM/sub structure. From Figure 3(a_3) it is seen that the EFC of the SP^3 mode (black curve) is different from the EFCs of SP^2s of the suspended A2DM sheet (blue curve) and the A2DM/sub structure (red curve) but resembles the red curves in Figure S2(a_2). It can therefore be concluded that the SP^3s of the A2DM/hBN/sub structure at $\lambda = 8$ μm have a σ-near-zero topology. The density plot [Figure 3(b_3)] shows that in this case all the wavenumbers in the EFC are involved in the mode excitation. The comparison of Figure 3(c_3) with Figure S2(c_3) (anisotropic topology) and Figure S2(c_2) (σ-near-zero topology) gives further evidence that the dispersion topology of the SP^3s of the A2DM/hBN/sub structure at $\lambda = 8$ μm is predominantly σ-near-zero rather than anisotropic. The direction of energy propagation corresponding to the white dashed line in Figure 3(d_3) is given by the angle $\varphi = 14.57°$, which coincides with the value obtained from Figure 2(d_2) and confirms the same topology of the modes.

The performed analysis shows that the presence of hBN in the case of $n = 10^{14}$ cm^{-2} leads to: (i) a change in the dispersion topology of the modes within the type-II RS band and outside of it for $\lambda > 7.3$ μm; (ii) the appearance of the modal features of the SP^2s of the suspended A2DM sheet and the A2DM/sub structure [c.f. Figures 2, 3, and Figure S2]; and (iii) the support of HP^3 modes inside the type-II RS band of hBN that possess the features of both the SP^2s of A2DM and the HP^2s of hBN. These findings may enhance the interaction of A2DM/hBN heterostructures with light and improve their performance in asymmetric guiding, beaming, and unidirectional propagation, as will be discussed in the next section.

3.3 Light–matter interaction, asymmetric guiding, beaming, and unidirectionality

As the Purcell effect explains [49], when an excited emitter — e. g., an atom, molecule, or quantum dot — is placed near a system that supports photonic modes, its lifetime changes as compared to the emission in free space. The strength of this effect, determined by the ratio of the quality factor to the volume of the available photonic modes, can be characterized by the spontaneous emission rate (SER) [50]

$$SER = \frac{P}{P_0} = 1 + \frac{6\pi}{\beta_0}\frac{\vec{\mu}_p}{|\vec{\mu}_p|}\cdot \mathrm{Im}\left[\bar{\bar{G}}_s\left(\vec{r}_0,\ \vec{r}_0,\ \omega\right)\right]\cdot\vec{\mu}_p, \tag{17}$$

where P and P_0 are the powers generated by the emitter with and without the structure, $\vec{\mu}_p$ and $\vec{r}_0$ define the orientation and position of the emitter, and $\bar{\bar{G}}_s(\vec{r}_0, \vec{r}_0, \omega)$ is the scattering term of the Green function of the system.

Owing to the support of subwavelength mode volumes by nanophotonic structures (e.g., by graphene-based structures), the light–matter interaction and thus the SER in their vicinity are enhanced. It has been reported that BP [7] and hBN [36] exhibit high SERs for materials with in-plane and out-of-plane hyperbolic dispersions. The enhancement in spontaneous emission of a quantum emitter is observed due to the considerable increase in the local density of states (LDOS) which is a result of the support of high-β modes by hyperbolic materials. Much like graphene, which is an isotropic 2D plasmonic material [51, 52], BP can also considerably enhance spontaneous emission of a quantum emitter outside of its hyperbolic region due to the support of surface plasmons [7].

Figure 4 illustrates the impact of an hBN buffer layer between the A2DM sheet and the substrate on the SER of a z-oriented point dipole located 10 nm above the A2DM sheet. Solid blue and red spectra are the SERs of the emitter for $n = 3 \times 10^{13}$ cm^{-2} and 10^{14} cm^{-2}, respectively. The lower electron densities are seen to result in higher SERs. The black dash-dotted spectra show that the SER of the source placed above the hBN/sub structure is considerably enhanced inside the type-II RS band of hBN, due to the excitation of the HP^2 modes (hyperbolic phonon polaritons). The presence of a 20-nm-thick hBN layer in the A2DM/hBN/sub structure is seen to decrease the SER of the source for both values of the electron density [c.f. the dashed and solid spectra in Figure 4(a)]. The increase of the hBN layer thickness to 100 nm considerably enhances the SER, as evidenced by the comparison of the dashed spectra in the two panels. For this thickness the SERs in the vicinity of the A2DM/hBN/sub structure are comparable to or even higher than the SERs near the A2DM/sub structure. Therefore, in case broadband enhancement of spontaneous emission is concerned, the thickness of the hBN layer is an important parameter. This broadband enhancement may not be achieved by graphene/hBN heterostructures [36]. Consequently, as far as, both enhanced light–matter interactions and guiding functionalities are concerned, A2DM/hBN/sub heterostructure can be a better candidate than the A2DM/sub structure.

Using a uniform graphene sheet modulated by a closely located corrugated ground plane [8], a patterned graphene sheet or a patterned BP layer [4, 5, 9], one can obtain a uniaxially anisotropic surface conductivity i.e., metasurface. This uniaxially anisotropic conductivity enables the realization of hyperlensing [4, 5, 8] and canalization [9] regimes. The hyperlensing regime allows transferring subwavelength images from a source point to an image point without diffraction while canalization makes possible diffractionless beaming of single subwavelength-scale confined rays. Similar functionalities have been reported in the visible range for periodic metallic gratings [12, 13]. It is also known that gapped Dirac materials such as bilayer graphene and transition metal dichalcogenides behave as chiral optical media under the illumination with circularly polarized light [14]. For these materials SP^2s are reciprocal while the edge modes are nonreciprocal. The nonreciprocal behavior becomes more pronounced with the increase of the off-diagonal component of the conductivity tensor of the material [14, 15].

Consider a double heterostructure composed of an A2DM/sub structure for $x < 0$ and an A2DM/hBN/sub structure for $x > 0$, which is shown at the top of Figure 5. The A2DM sheet covers the entire heterostructure and is located on a 20-nm-thick hBN layer. The two point dipoles exciting the heterostructure are separated by distance d and located in plane $x = 0$ (white dashed line) above the A2DM sheet.

The electric field distributions plotted in Figure 5 for different wavelengths and electron densities in A2DM illustrate how the hBN buffer layer leads to the asymmetry in the excitation of the modes. This effect enables asymmetric guiding, beaming, and unidirectionality of the guided modes supported by a uniform sheet of A2DM. The field distributions are shown for the most illustrative wavelengths and two electron concentrations. The mode profiles in Figure 5(a_1)–(e_1) agree well with the mode profiles in Figure 3 for $x > 0$ and in Figuree S2 for $x < 0$. It is seen from Figure 5(a_1) that at $\lambda = 5\ \mu m$ the mode profiles on both sides of the white dashed line are similar, featuring hyperbolic rays that show symmetric guiding in the A2DM/hBN/sub and A2DM/sub structures.

From the mode profiles in Figure 5(b_1) one can see that the topology of the guided modes in both parts of the heterostructure is σ-near-zero. At this wavelength, SP^2 modes are supported by the A2DM/sub structure and HP^3 modes are supported by the A2DM/hBN/sub structure. Therefore, the guided modes traveling in the plane of the A2DM sheet at $\lambda = 6.4$ μm are asymmetric with respect to plane $x = 0$. This asymmetry, caused by the presence of the hBN layer for $x > 0$, will be referred to as the asymmetric guiding of the modes. A similar asymmetric guiding can be observed for the modes of a truncated chiral 2D material [14, 15].

The asymmetric guiding becomes more pronounced for $\lambda = 6.6$ μm [Figure 5(c_1)]. At this wavelength the SP^2 guided mode travels in the region $x < 0$ with the σ-near-zero topology while the anisotropic HP^3 mode in the region

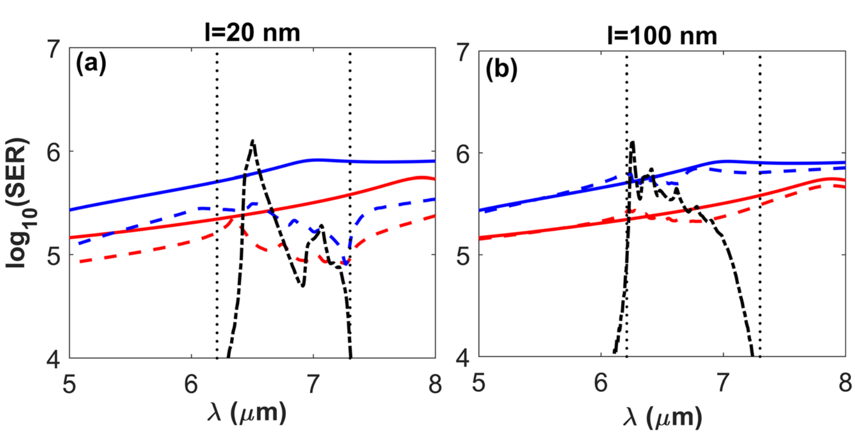

Figure 4: SERs of quantum emitter located 10 nm above A2DM/sub structure (solid curves) and A2DM/hBN/sub structure (dashed curves) with 20- and 100-nm-thick hBN layers for $n = 3 \times 10^{13}$ cm^{-2} (blue curves) and $n = 10^{14}$ cm^{-2} (red curves). Dash-dotted curves show SERs of emitter above similar hBN/sub structures; dotted vertical lines mark the boundaries of the type-II RS band of hBN.

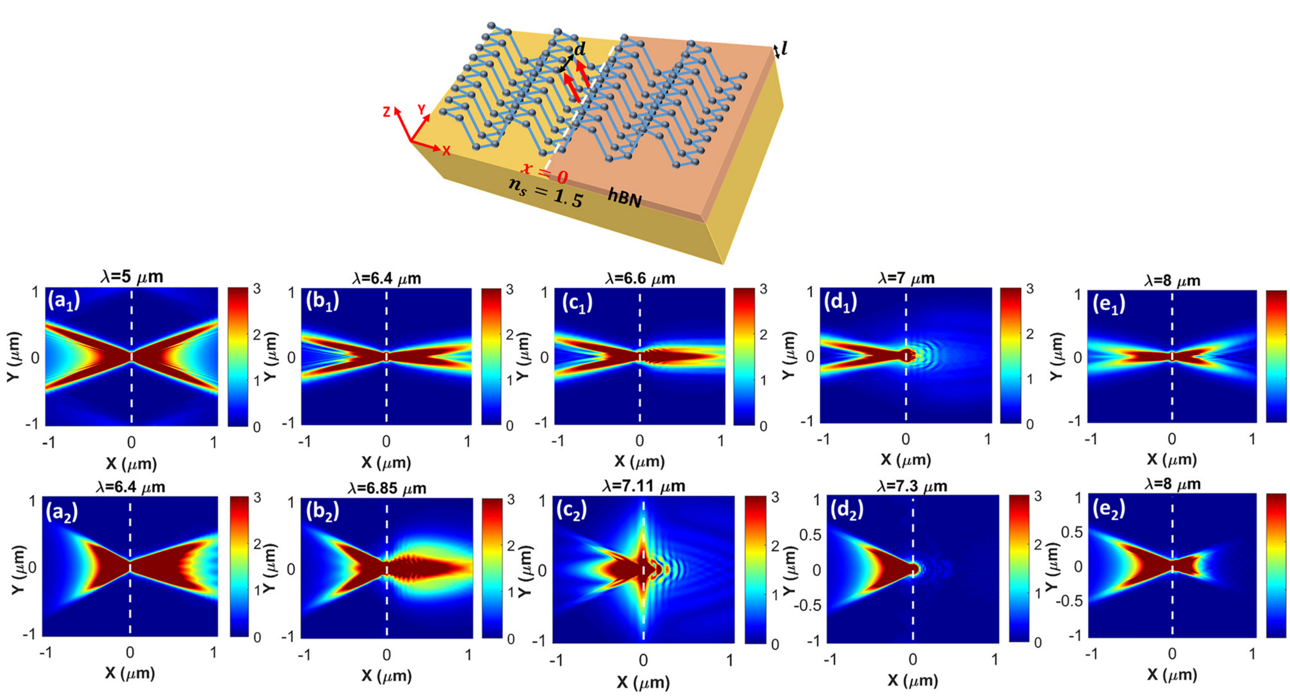

Figure 5: (top) Double heterostructure composed of A2DM/sub structure for $x < 0$, A2DM/hBN/sub structure with $l = 20$ nm for $x > 0$, and a uniform A2DM sheet on top of them, and (bottom) density plots of electric field $|\boldsymbol{E}|$ at different wavelengths for [(a_1)–(e_1)] $n = 10^{14}$ cm^{-2} and [(a_2)–(e_2)] $n = 3 \times 10^{13}$ cm^{-2}. A pair of z-oriented electric dipoles (red arrows) are 30 nm apart and 10 nm above the A2DM sheet. Vertical dashed lines show the boundary between the A2DM/sub and A2DM/hBN/sub structures.

$x > 0$ exhibits strong beaming in the $+x$ direction. A similar effect can be observed for a pair of different adjacent 2D anisotropic media [9].

The most extreme asymmetry in the propagation of the two modes is illustrated for $\lambda = 7$ μm by Figure 5(d_1). One can see that the propagation of the HP³ mode in this case is blocked for $x > 0$, whereas the SP² mode can still unidirectionally propagate in the region $x < 0$. The unidirectionality of propagation can be also observed for a uniform sheet of A2DM excited by an appropriately driven elliptically polarized electric dipole [16, 17]. The effect of asymmetric guiding is also present in Figure 5(e_1), because the dispersion topologies of the SP³ and SP² modes propagating for $x > 0$ and $x < 0$, respectively, are the same as in Figure 5(c_1).

The same conclusions regarding the asymmetric guiding, beaming, and unidirectionality can be drawn from the mode profiles in Figure 5(a_2)–(e_2). In this case a special consideration should be given to the symmetric edge mode of the uniform A2DM sheet that is confined to the y axis [white dashed line in Figure 5(c_2)]. The symmetric edge modes are usually confined to the truncated edge of an A2DM, e. g., a truncated layer of BP [15, 28] or graphene-based heterostructures [53, 54]. However, Figure 5(c_2) gives strong evidence that the edge modes with symmetric features can be supported by a uniform A2DM sheet of the considered double heterostructure as well. It is worth mentioning that in addition to the in-plane nanophotonics applications, similar to the graphene-based structures [55–57], metasurfaces and metamaterials based on A2DMs can also find practical applications. However, their investigations is out of the scope of this study.

4 Conclusion

We have analyzed the MIR features of hybrid guided modes supported by suspended sheet of A2DM, A2DM/sub, and A2DM/hBN/sub structures. The analysis of analytically derived exact dispersion relations was complemented by numerical simulations. We discovered that hybridization of the modes of the A2DM and hBN modes in the A2DM/hBN/sub heterostructure can lead to topological transitions for the hybrid modes inside the type-II RS band of hBN. These topological transitions enhance the guiding properties of the A2DM/hBN/sub heterostructure as compared to the A2DM/sub structure. It was shown that at the lateral interface of the A2DM/hBN/sub and the A2DM/sub structures, theirs hybrid modes feature asymmetric guiding, beaming, and unidirectional excitation upon their propagation along the A2DM sheet. We also demonstrated that, for appropriately taken thickness of the hBN layer, the

SER values of a point source placed close to the surface of the A2DM/hBN/sub heterostructure can be as large as those of the A2DM/sub structure. This feature – which is a consequence of the support of the hybrid modes and the commensurate increase in the local density of the photonic states – makes A2DM/hBN/sub heterostructure advantageous for both guiding and light–matter interaction purposes. The designed structures may explore the tunable functions of light–matter interactions in the MIR range and asymmetric in-plane anisotropic polariton nanophotonics.

Acknowledgments: Authors acknowledge financial support from DPT-HAMIT and TUBITAK projects under Nos. 113E331 and 109E301, and the Russian Science Foundation (Grant No. 19-13-00332). One of the authors (E.O.) also acknowledges partial support from the Turkish Academy of Sciences.

References

[1] A. V. Kildishev, A. Boltasseva, and V. M. Shalaev, "Planar photonics with metasurfaces," *Science*, vol. 339, p. 1232009, 2013.
[2] Y. Liu and X. Zhang, "Metasurfaces for manipulating surface plasmons," *Appl. Phys. Lett.*, vol. 103, p. 141101, 2013.
[3] A. A. High, R. C. Devlin, A. Dibos, et al., "Visible-frequency hyperbolic metasurface," *Nature*, vol. 522, p. 192–196, 2015.
[4] J. S. Gomez-Diaz, M. Tymchenko, and A. Alù, "Hyperbolic plasmons and topological transitions over uniaxial metasurfaces," *Phys. Rev. Lett.*, vol. 114, 233901, 2015.
[5] J. S. Gomez-Diaz, M. Tymchenko, and A. Alù, "Hyperbolic metasurfaces: surface plasmons, light-matter interactions, and physical implementation using graphene strips [Invited]," *Opt. Mat. Express*, vol. 5, p. 2313–2329, 2015.
[6] J. S. Gomez-Diaz and A. Alù. "Flatland optics with hyperbolic metasurfaces," *ACS Photonics*, vol. 3, p. 2211–2224, 2016.
[7] D. Correas-Serrano, J. S. Gomez-Diaz, A. Alvarez Melcon, and A. Alù, "Black phosphorus plasmonics: anisotropic elliptical propagation and nonlocality-induced canalization," *J. Opt.*, vol. 18, p. 104006, 2016.
[8] E. Forati, G. W. Hanson, A. B. Yakovlev, and A. Alù, "Planar hyperlens based on a modulated graphene monolayer," *Phys. Rev. B*, vol. 89, p. 081410, 2014.
[9] D. Correas-Serrano, A. Alù, and J. S. Gomez-Diaz, "Plasmon canalization and tunneling over anisotropic metasurfaces," *Phys. Rev. B*, vol. 96, p. 075436, 2017.
[10] A. Nemilentsau, T. Low, and G. Hanson, "Anisotropic 2D materials for tunable hyperbolic plasmonics," *Phys. Rev. Lett.*, vol. 116, p. 066804, 2016.
[11] S. A. Hassani Gangaraj, T. Low, A. Nemilentsau, and G. W. Hanson, "Directive surface plasmons on tunable two-dimensional hyperbolic metasurfaces and black phosphorus: green's function and complex plane analysis," *IEEE Trans. Antennas Propag.*, vol. 65, p. 1174, 2017.
[12] Y. Yang, L. Jing, L. Shen, et al., "Hyperbolic spoof plasmonic metasurfaces," *NPG Asia Mater.*, vol. 9, p. e428, 2017.
[13] C. L. Cortes and Z. Jacob, "Super-Coulombic atom–atom interactions in hyperbolic media," *Nat. Commun.*, vol. 8, p. 14144, 2017.
[14] A. Kumar, A. Nemilentsau, K. Hung Fung, G. Hanson, N. X. Fang, and T. Low, "Chiral plasmon in gapped Dirac systems," *Phys. Rev. B*, vol. 93, p. 041413, 2016.
[15] A. Nemilentsau, T. Low, and G. Hanson, *Chiral and Hyperbolic Plasmons in Novel 2-D Materials in Carbon-Based Nanoelectromagnetics*, Elsevier, 2019, p. 119–138.
[16] A. Nemilentsau, T. Stauber, G. Gómez-Santos, M. Luskin, and T. Low, "Switchable and unidirectional plasmonic beacons in hyperbolic two-dimensional materials," *Phys. Rev. B*, vol. 99, p. 201405, 2019.
[17] S. A. Hassani Gangaraj, G. W. Hanson, M. G. Silveirinha, K. Shastri, M. Antezza, and F. Monticone, "Unidirectional and diffractionless surface plasmon polaritons on three-dimensional nonreciprocal plasmonic platforms," *Phys. Rev. B*, vol. 99, p. 245414, 2019.
[18] H. Zhang, "Ultrathin two-dimensional nanomaterials," *ACS Nano*, vol. 9, p. 9451, 2015.
[19] H. Liu, A. T. Neal, Z. Zhu, et al., "An unexplored 2d semiconductor with a high hole mobility," *ACS Nano*, vol. 8, p. 4033, 2014.
[20] T. Low, R. Roldán, H. Wang, et al., "Plasmons and Screening in monolayer and multilayer black phosphorus," *Phys. Rev. Lett.*, vol. 113, p. 106802, 2014.
[21] E. van Veen, A. Nemilentsau, A. Kumar, et al., "Tuning two-dimensional hyperbolic plasmons in black phosphorus," *Phys. Rev. Applied*, vol. 12, p. 014011, 2019.
[22] L. Li, Y. Yu, G. J. Ye, et al., "Black phosphorus field-effect transistors," *Nat. Nanotechnol.*, vol. 9, p. 372, 2014.
[23] A. S. Rodin, A.o Carvalh, and A. H. Castro Neto, "Strain-induced gap modification in black phosphorus," *Phys. Rev. Lett.*, vol. 112, p. 176801, 2014.
[24] J. Qiao, X. Kong, Z. X. Hu, F. Yang, and W. Ji, "High-mobility transport anisotropy and linear dichroism in few-layer black phosphorus," *Nat. Commun.*, vol. 5, p. 4475, 2014.
[25] T. Low, A. S. Rodin, A. Carvalho, et al., "Tunable optical properties of multilayer black phosphorus thin films," *Phys. Rev. B*, vol. 90, p. 075434, 2014.
[26] C. Lin, R. Grassi, T. Low, and A. S. Helmy, "Multilayer black phosphorus as a versatile mid-infrared electro-optic material," *Nano Lett.*, vol. 16, p. 1683, 2016.
[27] Z. Liu and K. Aydin, "Localized surface plasmons in nanostructured monolayer black phosphorus," *Nano. Lett.*, vol. 16, p. 3457, 2016.
[28] Z. Bao, H. Wu, and Y. Zhou, "Edge plasmons in monolayer black phosphorus," *Appl. Phys. Lett.*, vol. 109, p. 241902, 2016.
[29] H. Lin, B. Chen, S. Yang, et al., "Photonic spin Hall effect of monolayer black phosphorus in the Terahertz region," *Nanophotonics*, vol. 7, p. 1929–1937, 2018.
[30] P. Chen, C. Argyropoulos, M. Farhat, and J. S. Gomez-Diaz, "Flatland plasmonics and nanophotonics based on graphene and beyond," *Nanophotonics*, vol. 6, p. 1239–1262, 2017.
[31] J. D. Caldwell, L. Lindsay, V. Giannini, et al., "Low-loss, infrared and terahertz nanophotonics using surface phonon polaritons," *Nanophotonics*, vol. 4, p. 44–68, 2015.
[32] S. Foteinopoulou, G. C. R. Devarapu, G. S. Subramania, S. Krishna, and D. Wasserman, "Phonon-polaritonics: enabling

powerful capabilities for infrared photonics," *Nanophotonics*, vol. 8, p. 2129–2175, 2019.
[33] J. D. Caldwell, A. V. Kretinin, Y. Chen, et al., "Sub-diffractional volume-confined polaritons in the natural hyperbolic material hexagonal boron nitride," *Nat. Commun.*, vol. 5, p. 5221, 2014.
[34] S. Dai, Z. Fei, Q. Ma, et al., "Tunable phonon polaritons in atomically thin van der waals crystals of boron nitride," *Science*, vol. 343, p. 1125–1129, 2014.
[35] S. Dai, Q. Ma, M. K. Liu, et al., "Graphene on hexagonal boron nitride as a tunable hyperbolic metamaterial," *Nat. Nanotechnol.*, vol. 10, p. 682, 2015.
[36] A. Kumar, T. Low, K. H. Fung, P Avouris, and N. X. Fang, "Tunable light–matter interaction and the role of hyperbolicity in graphene–hBN system," *Nano Lett.*, vol. 15, p. 3172, 2015.
[37] H. Hajian, A. Ghobadi, B. Butun, and E. Ozbay, "Tunable, omnidirectional, and nearly perfect resonant absorptions by a graphene-hBN-based hole array metamaterial," *Opt. Express*, vol. 26, p. 16940, 2018.
[38] H. Hajian, A. Ghobadi, A. E. Serebryannikov, B. Butun, G. A. E. Vandenbosch, and E. Ozbay, "VO2-hBN-graphene-based bi-functional metamaterial for mid-infrared bi-tunable asymmetric transmission and nearly perfect resonant absorption," *J. Opt. Soc. Am. B*, vol. 36, p. 1607, 2019.
[39] P. Li, I. Dolado, F. J. Alfaro-Mozaz, et al., "Infrared hyperbolic metasurface based on nanostructured van der Waals materials," *Science*, vol. 359, p. 892, 2018.
[40] W. Ma, P. Alonso-González, S. Li, et al., "In-plane anisotropic and ultra-low-loss polaritons in a natural van der Waals crystal," *Nature*, vol. 562, p. 557–562, 2018.
[41] Z. Zheng, N. Xu, S. L. Oscurato, et al., "A mid-infrared biaxial hyperbolic van der Waals crystal," *Sci. Adv.*, vol. 5, p. eaav8690, 2019.
[42] C. R. Dean, A. Young, I. Meric, et al., "Boron nitride substrates for high-quality graphene electronics," *Nature Nanotech.*, vol. 5, p. 722, 2010.
[43] X. Cui, G. Lee, Y. D. Kim, et al., "Multi-terminal transport measurements of MoS2 using a van der Waals heterostructure device platform," *Nat. Nanotech.*, vol. 10, p. 534, 2015.
[44] K. Chaudhary, M. Tamagnone, M. Rezaee, et al., "Engineering phonon polaritons in van der Waals heterostructures to enhance in-plane optical anisotropy," *Sci. Adv.*, vol. 5, p. eaau7171, 2019.
[45] I. D. Rukhlenko, A. Pannipitiya, M. Premaratne, and G. P. Agrawal, "Exact dispersion relation for nonlinear plasmonic waveguides," *Phys. Rev. B*, vol. 84, p. 113409, 2011.
[46] I. D. Rukhlenko, M. Premaratne, and G. P. Agrawal, "Guided plasmonic modes of anisotropic slot waveguides," *Nanotechnology*, vol. 23, p. 444006, 2012.
[47] H. Hajian, I. D. Rukhlenko, P. T. Leung, H. Caglayan, and E. Ozbay, "Guided plasmon modes of a graphene-coated Kerr slab," *Plasmonics*, vol. 11, p. 735, 2016.
[48] G. W. Hanson, "Dyadic Green's functions for an anisotropic, non-local model of biased graphene," *IEEE Trans. Antennas Propag.*, vol. 56, p. 747, 2008.
[49] E. M. Purcell, H. C. Torrey, and R. V. Pound, "Resonance absorption by nuclear magnetic moments in a solid," *Phys. Rev.*, vol. 69, p. 37, 1946.
[50] L. Novotny and B. Hecht, *Principles of Nano-Optics*, 2nd ed. Cambridge: Cambridge University Press, 2012.
[51] F. H. L. Koppens, D. E. Chang, and F. Javier García de Abajo, "Graphene plasmonics: a platform for strong light–matter interactions," *Nano Lett.*, vol. 11, p. 3370–3377, 2011.
[52] E. Forati, G. W. Hanson, and S. Hughes, "Graphene as a tunable THz reservoir for shaping the Mollow triplet of an artificial atom via plasmonic effects," *Phys. Rev. B*, vol. 90, p. 085414, 2014.
[53] Z. Fei, M. D. Goldflam, J. S. Wu, et al., "Edge and surface plasmons in graphene nanoribbons," *Nano Lett.*, vol. 15, p. 8271, 2015.
[54] X. Guo, H. Hu, D. Hu, et al., "High-efficiency modulation of coupling between different polaritons in an in-plane graphene/hexagonal boron nitride heterostructure," *Nanoscale*, vol. 11, p. 2703–2709, 2019.
[55] S. Quader, J. Zhang, M. R. Akram, and W. Zhu, "Graphene-based high-efficiency broadband tunable linear-to-circular polarization converter for terahertz waves," *IEEE J. Selected Topics Quan. Elect.*, vol. 26, p. 4501008, 2020.
[56] J. Zhang, X. Wei,I. D. Rukhlenko, H.-T. Chen, and W. Zhu, "Electrically tunable metasurface with independent frequency and amplitude modulations," *ACS Photonics*, vol. 7, p. 265, 2020.
[57] J. Zhang, X. Wei, M. Premaratne, and W. Zhu, "Experimental demonstration of electrically tunable broadband coherent perfect absorber based on graphene-electrolyte-graphene sandwich structure," *Photonics. Res.*, vol. 7, p. 868, 2019.

Supplementary material: The online version of this article offers supplementary material https://doi.org/10.1515/nanoph-2020-0080.